Synthesis and characterization of 3D-printable geopolymeric foams for thermally efficient building envelope materials

Hussam Alghamdi*, Narayanan Neithalath**

Abstract

Synthesis and characterization of 3D-printable foamed fly ash-based geopolymer matrices for thermal insulation is the focus of this paper. A surfactant-based foaming process, multi-step mixing that ensures foam jamming transition and thus a dry foam, and microstructural packing to ensure adequate skeletal density are implemented to develop foamed suspensions amenable to 3D-printing. The foamed suspensions show lower yield stress with increasing surfactant contents, especially above the foam jamming transition. The mixtures demonstrate adequate extrudability, shape retention, and buildability. The geopolymeric foams show porosities ranging from 55 to 75% and bulk densities from 0.6 to 1.0 g/cm³, and these properties are similar irrespective of whether the mixtures are extruded or conventionally cast. The thermal conductivities of the foamed matrices range from 0.15 to 0.25 W/m-K. It is shown that designed architectures that minimize heat transfer can be printed using foamed matrices to obtain sandwich wall panels with thermal insulation properties comparable to or better than those of currently available insulated concrete wall panels. This positions 3D-printing as a strategy to develop composite systems with previously unattainable thermal performance.

Keywords: 3D-printing; Fly ash; Surfactant; Geopolymeric foam; Porosity; Rheology; Yield stress; Buildability.

^{*} Graduate student, School of Sustainable Engineering and Built Environment, Arizona State University, Tempe AZ 85287

^{†,*} Professor, School of Sustainable Engineering and Built Environment, Arizona State University, Tempe AZ 85287; Corresponding Author (Phone: +1-480-965-6023; Fax: +1-480965-0557; e-mail: Narayanan.Neithalath@asu.edu)

1. Introduction

3D-printing or additive manufacturing (AM) is gaining prominence in the construction industry. One of the unique attributes of 3D-printing is the capability to implement complex architectural shapes [1–4]. Furthermore, 3D-printing technology has been shown to result in a reduction in construction cost and time due to the avoidance of formwork and reduced on-site labor [5,6]. Among the many 3D-printing techniques for cementitious materials, material extrusion followed by layered printing is the most commonly used technique [4,7–12]. The importance of rheological characteristics of cementitious binders in ensuring smooth flow through the extrusion system without material inhomogeneities and the requirements in terms of yield stress for buildability have been detailed in several recent publications [4,13–16].

The use of concrete 3D-printing for architectural and structural elements have been widely discussed in recent literature [1–4,17–20]. Building envelopes printed using concrete have appeared as demonstration structures in different parts of the world. This paper synergizes the use of 3D-printing and material design of porous cementitious foam for specific building functions – in this case, thermal insulation. Thermal insulation materials reduce the heat gain/loss through building envelopes and it is one of the best approaches to enhance building energy efficiency. Porous materials find extensive applications in building insulation. This study envisages 3D-printed cementitious foams in lieu of conventional building insulation materials such as extruded polystyrene, mineral wool etc. that can be placed in between the concrete layers of a typical insulated precast concrete wall panel (sandwich wall panel). The fire resistance and environmental sustainability of many of the commonly used insulation materials are questionable [21– 23], which can be overcome by the proposed approach. The concrete wall panels can also be 3D-printed if desired, resulting in a co-printed envelope system consisting of the structural and insulating components. While cementitious foams are significantly more insulating than solid concrete, they still exhibit thermal conductivity values that are higher than commercial insulating materials mentioned above. This drawback can be overcome by designing specific architectures using the 3D-printed cementitious foams. A conceptual representation of such a design idea and laboratory prototypes are shown in Figure 1. The porous foams can be printed in such a way that the composite structure has an overall void volume fraction (excluding the voids in the foam) of 40-80% depending on the desired thermal conductivity of the envelope. Thus, the composite structure becomes a dual-porosity medium, with smaller pores in the foam and larger pores in between the printed paths. By proper design of the insulating layer architecture and numerical simulations of heat transfer, issues such as thermal bridges which affect the dynamic thermal performance of sandwich wall panels can also be eliminated. The desired layer architecture (examples of which are shown in Figure 1) can only be created using 3D printing, which is an important advantage over conventionally cast cementitious foams. The layer geometry can also be optimized for enhanced structural-thermal performance, which also cannot be accomplished using conventional casting of foams. Thus, this paper lays the foundation for material and geometric design of 3D printable cementitious foams. The emphasis of this paper, however, is the material design of 3D-printable, sustainable cementitious foams and its microstructural/thermal characterization.

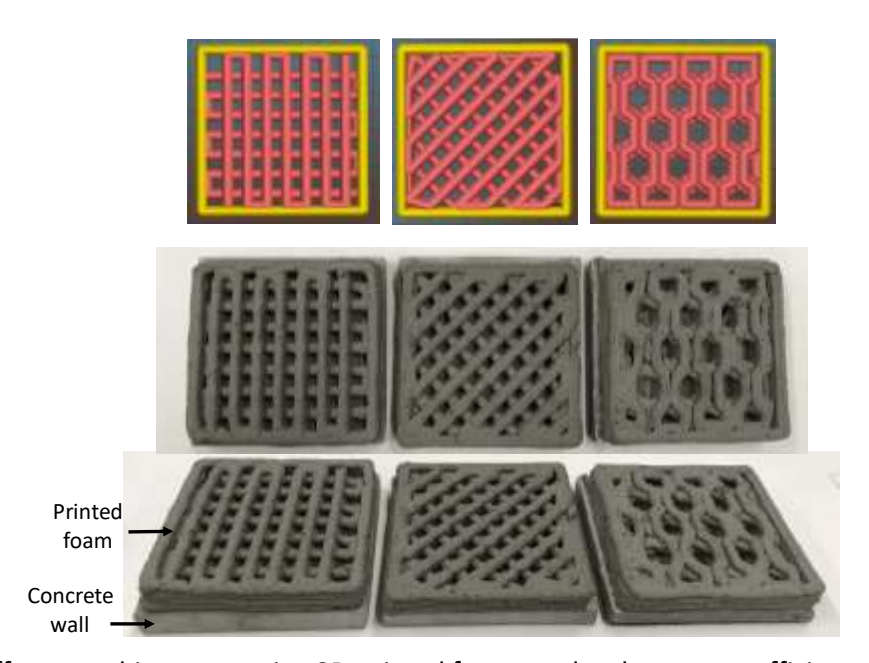


Figure 1: Different architectures using 3D-printed foams to develop energy efficient composite envelope systems. The 3D-printed insulation here has a void volume fraction of 0.50 (excluding the voids in the geopolymeric foam itself).

Past studies have reported the use of 3D-printing to fabricate porous materials from different starting materials for many applications such as water filtration, catalysis, biomedical scaffolds, and lightweight structural elements [24–31]. In this study, the foamed matrix is designed using alkali activated fly ash to ensure economical, sustainable, and lightweight matrices. While several chemical foaming agents including hydrogen peroxide, alumina powder, metallic silicon, and recently sodium carbonate [32–34] have been used as foaming agents, this paper employs a physical foaming process using surfactants [32,35,36] that introduce homogeneous bubbles in the geopolymer matrix. The choice of a surfactant-based foaming process was based on the evaluation of bubble stability under extrusion-based 3D-printing. While the surfactant also stabilizes the air bubbles [37–40], unjammed (wet) foams are sometimes formed

because of the reduction in water-air surface tension [41]. Wet foams[‡] where the foam volume fraction is lower than the jamming transition are flowable and hence not amenable to 3D-printing. The jamming transition for 3D disordered foams is ~0.64 [42,43]. To ensure adequate skeletal density and cohesiveness of the mixtures to enable 3D-printing, and at the same time maintaining a higher porosity, the particle packing in the suspension is modified through the use of fine powders such as limestone. Moreover, a modified mixing procedure is employed to facilitate the formation of stable dry foams.

2. Experimental Program

2.1 Materials and Printing Parameters

A Class F fly ash conforming to ASTM C 618 was the major source material used in this study. To improve the printability (which includes extrudability, shape retention, and buildability) of the foamed suspension, additional materials such as ordinary portland cement (OPC), silica fume, and fine limestone powder were used based on our previous published work [10,11]. The chemical composition of all the source materials are listed in Table 1. Figure 2 shows the particle size distributions (PSD) of the source materials. The median particle sizes are 17.9 μm for the fly ash, 1.5 μm for limestone, and 11.2 μm for OPC, as determined from laser particle size analysis. The activation agents utilized in this study were sodium silicate solution (waterglass), sodium hydroxide (NaOH), or sodium sulfate (Na₂SO₄). Waterglass, supplied by PQ Corporation, has a solids content of 36%, a silica modulus (molar ratio of SiO₂-to-Na₂O) (M_s) of 3.3, and specific gravity of 1.38 g/cm³. NaOH was added to waterglass to lower the M_s and obtain the desired Na₂O-to-total powder (n) values. Sodium sulfate, which is a non-caustic activator, was used when a small amount of OPC was used in addition to fly ash as the binding material. More details of such mixture designs are available in [44]. Lightcrete 02TM surfactant liquid was used as a foaming agent and foam stabilizer.

A BCN3D Cartesian printer [10,11] was used in this study to print the foamed suspensions. All printing parameters including printing speed, layer width and height, and infill volume and pattern were adjusted using Slic3r software [45]. The printing parameters used in this study were: layer height of 3mm, layer width of 6 mm, and printing speed of 20 mm/s. The diameters of the barrel, die entry, and die exit were 35 mm, 10 mm, and 4 mm respectively.

-

[‡] The terms "wet" and "dry" foams do not reflect the literal meaning of the terms; in fact, these terms are used to denote volume fraction of foams below and above the foam jamming transition, respectively.

Table 1: Chemical composition of the source materials

Components of the hinders	Chemical composition (% by mass)							
Components of the binders	SiO ₂	Al_2O_3	Fe ₂ O ₃	CaO	MgO	SO ₃	LOI	
Fly Ash (F)	58.40	23.80	4.19	7.32	1.11	3.04	2.13	
Silica fume (S)	> 90.0	-	-	< 1.0	-	-	-	
OPC (C)	19.60	4.09	3.39	63.21	3.37	3.17	2.54	
Limestone (L), 1.5 μm	CaCO ₃ > 99%							

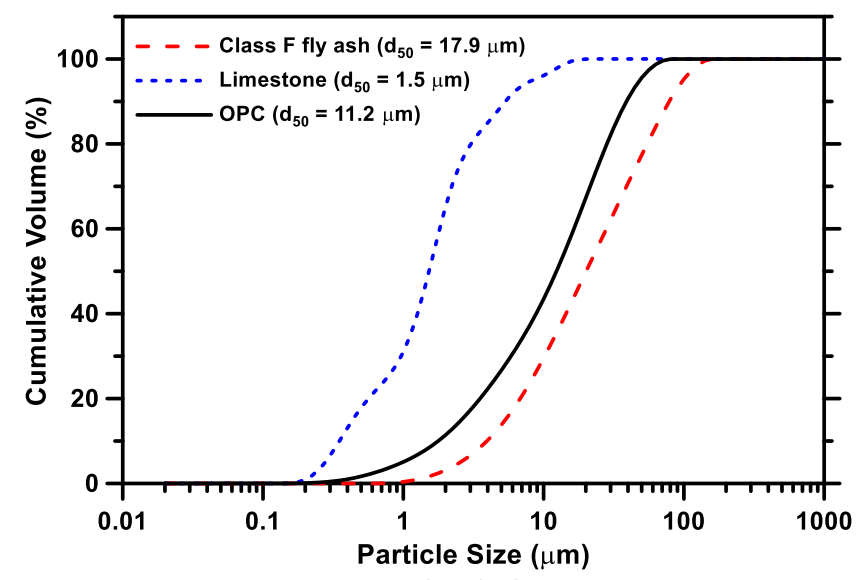


Figure 2: Particle size distributions (PSD) of the suspension constituents.

2.2 Preparation of the Printable Foamed Suspensions: Importance of the Mixing Procedure

The smooth extrusion of foamed suspensions through the nozzle and retention of the printed shape are the printability criteria adopted in this study towards material design. Since the mini-slump test can be used to indicate shape stability [10,11], it was utilized in the initial development of a family of alkaliactivated fly ash-based printable foamed suspensions.

A binder combination that contained 70% fly ash and 30% limestone powder (by mass) was chosen from a series of printable alkali-activated fly ash-based binders reported earlier [10], as a starting point. The amounts of sodium silicate and NaOH were adjusted to provide an activator with an M_s of 1.0. The ratio of Na_2O -to-total powder (n) was maintained at 0.07. Three different surfactant (S) dosages were used: 1, 2, and 3% by mass of the binder. A mass-based liquid-to-binder (I/b) ratio of 0.60 (including the liquid surfactant and the water content in the activator) was chosen. This was needed to avoid the stickiness of suspension due to the highly viscous alkali activator that reduces foam expansion and consequently the porosity [35]. This I/b also helped maintain appropriate workability and flowability of the foamed

suspension, at the same time ensuring buildability (which is quantified using viscosity recovery as described later). The activator solution and requisite amount of water were added to the binder and mixed at 200 rpm for 30 sec and then at 1200 rpm for 4.5 min until a homogeneous mixture was obtained. The surfactant was then added and mixed until a uniform mixture resulted. The resultant mixture was observed to be very soft (wet foam), resulting in a non-printable suspension (Figure 3(a)). It is likely that large and isolated bubbles were created, and the mixture had a foam volume fraction lower than the jamming transition of 0.64 [42,43] which resulted in instability. To obtain a stable, dry foam with a foam volume fraction at or near the jamming transition, this study developed a modified mixing procedure where water was added in a stepwise manner. In this procedure, the activator solution with a quarter of the total water requirement was added to the powder mixture and mixed at 200 rpm for 30 sec and then at 1200 rpm for 4.5 min until a homogenous mixture was obtained. Then the total amount of surfactant was added and mixed for further 10 min. This mixture has a high surfactant concentration. Subsequently, the remaining water was gradually added in three equal steps until the total amount of water was fully added and mixed for further approximately 3 mins during each step to disperse the foam. The formation of dry foam (jammed foam) along with a solid skeleton having adequate particle packing to ensure stability, resulted in a foamed suspension which was cohesive enough and demonstrated shape stability as shown in Figure 3(b).

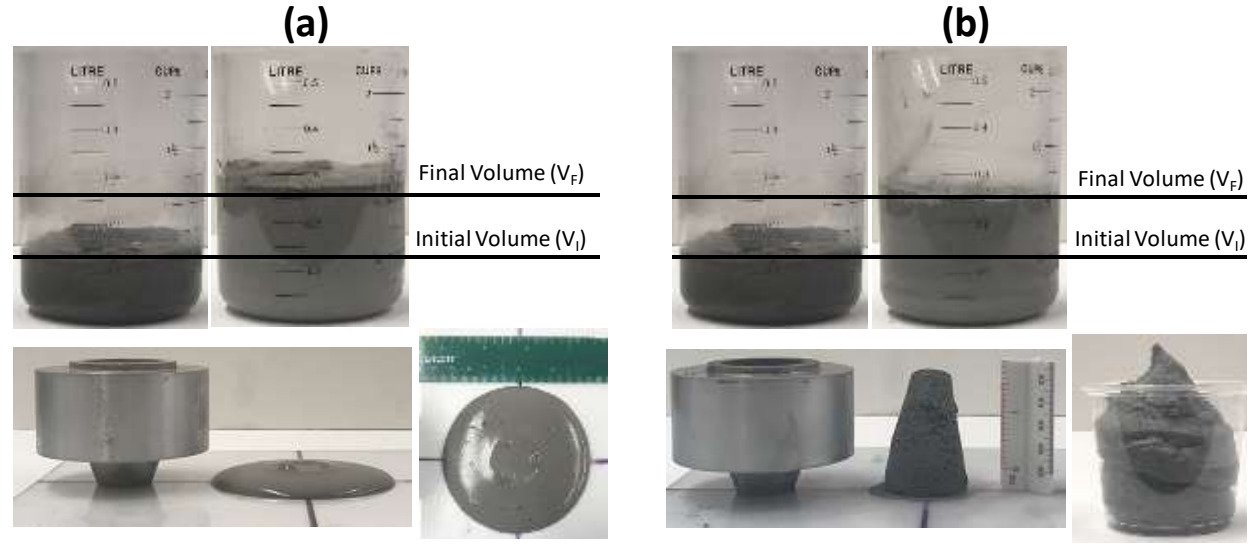


Figure 3: Shape stability as observed during: (a) the normal mixing procedure when all the water was added to the powder in a single step, and (b) the modified mixing procedure when the water was added to the powder in multiple steps.

Along with the binary suspension prepared from fly ash and limestone, silica fume and OPC were also used as minor ingredients to improve the particle packing and mechanical properties of the foamed

matrices. The fly ash – silica fume – limestone system was activated using a combination of NaOH and sodium silicate to provide a Na_2O -to-powder ratio (n) of 0.07 and an M_5 of 1.0. The fly ash – OPC – limestone system was activated using only Na_2SO_4 as reported in [44]. In the latter case, a cohesive and printable foamed suspension (dry foam) was obtained directly during mixing with a reduced amount of water (there was no need for adding more water to avoid the stickiness issue experienced in suspensions activated by highly alkaline activators). The fly ash – limestone (FL) and fly ash – limestone – silica fume (FLS) systems, were synthesized using the modified mixing procedure where the water was added in steps, while for the fly ash – limestone-cement (FLC) system, the activator and the requisite amount of water were added to the binder in a single step, followed by the surfactant and mixed for only 5 min. The final printable foamed suspensions are listed in Table 2. The third system is not strictly a geopolymer since OPC is used, but is compared to the two geopolymeric systems described above. All the printed shapes were cured for 24h at 70°C to enhance the polymerization reaction and the formation of products. After the curing duration, the compressive strengths tested on 50 mm side cubes ranged from 1.0 MPa to 6.5 MPa depending on the mixture proportion and surfactant content. The highest strengths were recorded for the FLC mixture.

Table 2: Binder proportions for the final printable suspensions.

	Binders (% by mass)				Sodium	NaOH +			Surfactant	
I ID I	FFA	LS	0.	OPC (C)	sulfate (%)	waterglass		Liquid/binder	(S)	
							Ms	ratio (by mass)	(% by mass of	
	(F)	(L)				n	IVIS		binder)	
FL	70	30	-	-	-	0.07	1.0	0.60	1, 2, 3	
FLS	60	20	20	-	-	0.07	1.0	0.65	1, 2, 3	
FLC	50	20	-	30	3	-	-	0.25	1, 2, 3	

2.3 Test Methods

2.3.1 Foam expansion and shape retention

Foam expansion (F_E) was determined as the increase in the suspension volume after mixing according to:

$$F_E \left(\%\right) = \left(\frac{V_F - V_I}{V_A} \times 100\right) \tag{1}$$

where, V_F is the final volume of the suspension after addition of the surfactant and V_I is the initial volume of the suspension that does not contain the surfactant.

Shape retention factor of printed filament (SRF) was determined to evaluate the layer stability of foamed suspensions in accordance with the procedure described in [46]. This factor is quantified as:

$$SRF = \left(\frac{Designed\ layer\ width\ of\ filament}{Actual\ printed\ layer\ width\ of\ filament}\right) \tag{2}$$

2.3.2 Rheological characterization

Mini-slump test was used to estimate the shape stability of the foamed suspensions. A mini slump cone with a bottom diameter of 38 mm, top diameter of 19 mm, and a height of 57 mm was used. A TA Instruments AR 2000EX dynamic shear rheometer was used to carry out parallel plate rheology tests. The rheometer was setup with Peltier elements for the bottom plate and conditioned to 25±0.1 °C. The upper and lower plates were serrated with a notch depth of 1 mm and 0.15 mm respectively to prevent slip on the shearing surface. The sample volume for a 2 mm plate gap was calculated and placed on the bottom plate to avoid an overfilled state while testing. The plate gap was chosen so as to ensure that it is at least 10 times larger than the largest bubble size. The following steps were employed in the rheology testing, as shown in Figure 4(a): (i) a stepped ramp-up pre-shear phase for approximately 80 s to homogenize the suspension, (ii) a stepped ramp-up phase for about 40 s, and (iii) a stepped ramp-down phase [47,48]. The data collected from the ramp-down phase was used in the analysis. Rheological parameters of the suspensions (apparent yield stress and plastic viscosity) were extracted from the relationship between shear stress and shear rate. The range of the shear rate used in this test was from 5-to-100 s⁻¹. The Y-intercept of this relationship was recorded as the Bingham yield stress and the slope as the plastic viscosity. The use of a Bingham model for foamed suspensions has been reported [49].

In addition, the parallel plate test was also carried out to measure viscosity recovery (suspension buildability). The buildability test was done in a sequence of steps that mimic extrusion-based 3D printing [46,50]. The steps employed include: (i) a stepped ramp-up pre-shear phase for approximately 80 s to homogenize the suspension, (ii) constant low shear rate of 0.01 s⁻¹ for 60 s to determine the initial viscosity of fresh suspensions before printing, (iii) constant high shear rate of 100 s⁻¹ for 30s which mimics the extrusion process, and (iv) constant low shear rate of 0.01 s⁻¹ for 60 s to determine the final viscosity of suspensions after extrusion printing. The experimental scheme is shown in Figure 4(b).

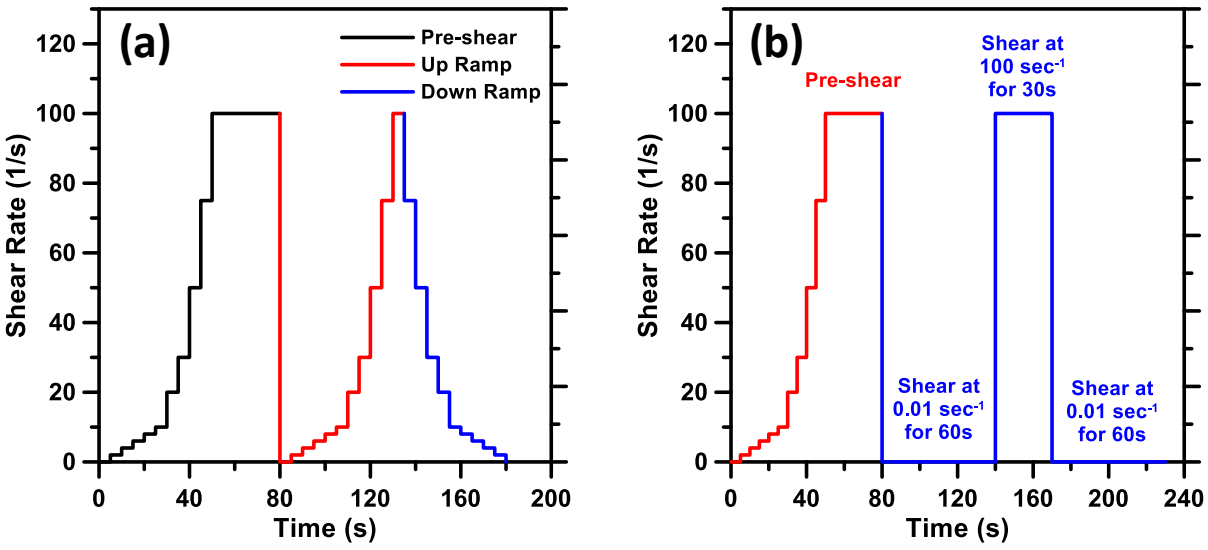


Figure 4: Parallel plate rheology test procedure to determine: (a) yield stress and plastic viscosity, and (b) plastic viscosity recovery of the suspensions for buildability.

2.3.3 Pore structure and microstructure of foamed matrices

The pore structure and the microstructure of the hardened foamed matrices were evaluated using Mercury Intrusion Porosimetry (MIP) and Scanning Electron Microscopy (SEM). For MIP experiments, small chunks of the foamed matrix were weighed and placed in the low-pressure chamber of the porosimeter (Quantachrome Instrument Pore Master). The sample was filled with mercury starting from ambient pressure to 345 kPa (60 psi) in this step. The sample was then placed in the high-pressure chamber and the applied pressure increased to 414 MPa (60,000 psi). The pore diameter (d) as a function of the intrusion pressure was obtained from the Washburn equation as:

$$d = \frac{-4\sigma\cos\theta}{\Delta P} \tag{3}$$

where ΔP is the difference in the pressure between successive steps (MPa), θ is the contact angle between mercury and the cylindrical pore (taken as 130° in this study) [51–53], and (σ) is the surface tension between mercury and the pore walls (0.485 N/m). To understand the effect of extrusion printing on the porosity and pore sizes of the foamed suspensions, two sets of samples were used. First, samples were obtained from the printed filaments to represent the influence of extrusion. Second, samples not influenced by extrusion effects were obtained from specimens that were conventionally poured and cast in a 25 mm x 50 mm cylinder mold.

A Nanoimages SNE-4500 Plus Table top scanning electron microscope operating in the secondary mode was used to image the microstructure. All the samples prepared for SEM imaging were gold sputtered before imaging under an operating voltage of 30 kV.

2.3.4 Physical and thermal properties of foamed matrices

The specific gravities of the foamed samples were determined using a gas pycnometer (Ultrapyc 1200e, Quantachrome Instruments). The thermal conductivity of the foamed samples was determined using the guarded hot plate method in accordance with ASTM C 177. Plain OPC paste plate samples (100 mm x 100 mm x 15 mm) were prepared at a w/c of 0.40 to be used as a reference. One layer of foamed suspension, 3 mm in thickness was printed on the aforementioned OPC plate to form a composite, and the thermal conductivity of the foam was determined from the composite thermal conductivity using a series rule of mixtures. 1D uniform heat flow is ensured by using thermally isolated guards surrounding the central metered section where the applied power is measured. Heat sinks located on the top and bottom of the apparatus dissipate the heat to ensure uniform temperatures at the outer surfaces of the specimen [54]. Thermal conductivity (k) was calculated using Fourier's equation as:

$$k = \frac{q L}{2 A (T_{hot} - T_{cold})} \tag{4}$$

where q is the power input to the heater, L is the thickness of the plate specimen, A is the surface area of the specimen, T_{hot} is the temperature of the hot surface, and T_{cold} is the temperature of the cold surface.

3. Results and Discussion

3.1 Foam Expansion and Rheological Characterization

Foam expansion and slump flow are important characteristics that define the early age properties of 3D-printable foamed suspensions. Figure 5(a) shows the foam expansion and Figure 5(b) shows the mini slump values of the foamed suspensions. Foam expansion increases with increasing surfactant content as expected. All three mixtures (FL, FLS, and FLC) expanded by ~100% (or doubled their volume) when 3% of surfactant powder (by mass) was used. Even with a significantly reduced water content, the FLC mixture shows comparable expansion to those of the other mixtures. The high viscosity of the activator solution necessitated a higher liquid content in FL and FLS mixtures for desirable expansion. The slump values shown in Figure 5(b) also demonstrate a similar trend as that of expansion. The higher the surfactant content, the higher the slump value, attributable to a lower suspension yield stress with increasing surfactant concentration [41,55], which is also shown in a forthcoming section of this paper. These mixtures demonstrated excellent consistency and smooth flow during extrusion. Generally, a higher

slump is beneficial in extrusion but not in shape stability, which is an important criterion for 3D printed elements. However, the foamed suspensions with relatively higher slump values were also successful in retaining their shapes because of their low densities.

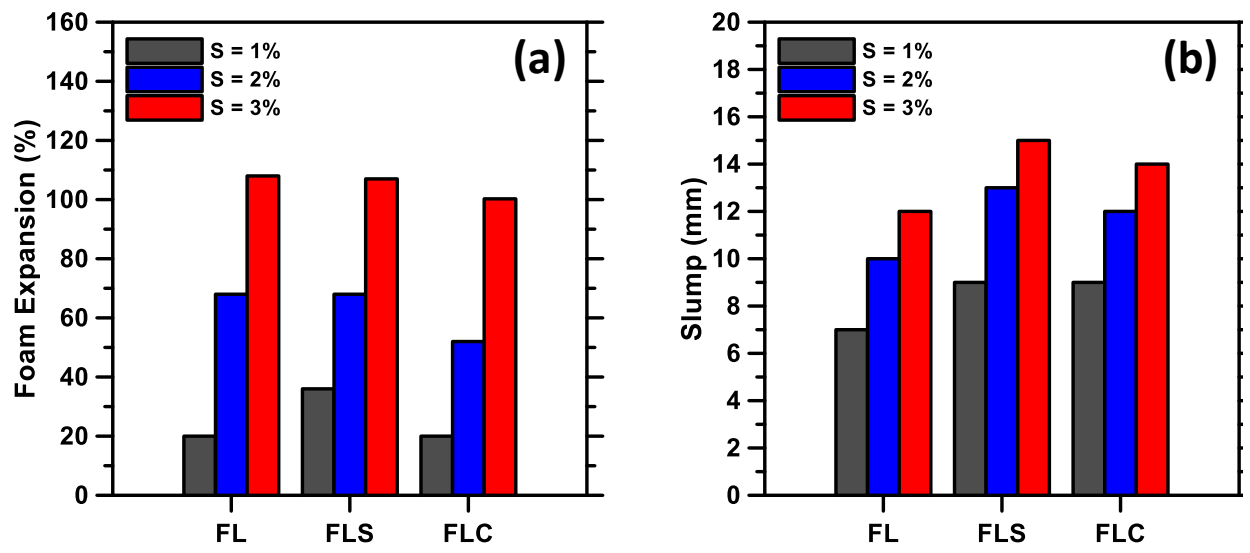


Figure 5: (a) Foam expansion and (b) slump values of the printable foamed suspensions.

Yield stress and plastic viscosity are important rheological parameters that have been used to evaluate the influence of starting materials and proportions on 3D printed binders [10,11,46,50]. Foams with void volume fractions greater than the jamming transition are known to be yield stress fluids, just as conventional cement pastes, and hence rheological techniques used for cement pastes can be safely used for dry foams. Thus, below the yield stress the foams behave as viscoelastic solids and above the yield stress as non-Newtonian fluids. Figure 6 shows the yield stress and plastic viscosity of printable foamed suspensions evaluated in this study using parallel plate rheometry, which is reported as the most appropriate tool to study bulk foam rheology [56]. The yield stress of FL, FLS, and FLC suspensions are similar at a given surfactant dosage, while plastic viscosity is found to be generally invariant with the suspension type and the surfactant dosage within the scope of materials and dosages used in this study. Foam viscosity is known to increase with decreasing bubble size and foam density. With an increase in surfactant dosage, bubble size increases (shown later through pore size distributions) and overall density decreases, plausibly negating their effects on changes in viscosity.

The yield stress of the foamed suspensions with low surfactant dosage (S = 1%) vary between 120 Pa and 130 Pa, while it is around 60 Pa for higher surfactant dosages (S = 2, and 3%). For foam volume fractions

up to around 50% (for e.g., the 1% surfactant mixture with a porosity of 55% – see a later section for porosity values), the yield stress of the foamed suspension has been reported to be similar to that of the paste that forms the skeleton [57]. The rheological response of the foamed sample can be considered to be a result of competition between the skeleton yield stress that tends to deform the bubbles and the capillary stress acting on the bubble surface that resists this deformation. The net effect can be expressed in terms of a plastic capillary number [57,58], C_p , expressed as:

$$C_p = \frac{\tau_y}{(2T/R)} \tag{5}$$

Here, τ_{v} is the yield stress of the foamed suspension, T is the surface tension and R is the bubble radius. Assuming that the surface tension scales between 0.06 N/m and 0.03 N/m between 1% and 3% surfactant dosage, and the bubble size ranges between 25 μ m and 100 μ m (see a later section on pore structure), the C_{p} value for the 1% surfactant dosage case is around 0.02 for all the three mixtures. For C_{p} values \sim 0.10 (i.e., surface tension is dominant), it has been shown that τ_{v} is invariant of foam volume fraction ϕ when $\phi \leq 0.50$ [57]. Thus, the yield stress of foamed samples is unaffected by the bubbles since the bubbles behave as rigid inclusions in the paste. However, for $\phi \geq 0.64$ (2% and 3% surfactant dosages), C_{p} increases to >0.10 and the bubbles behave as softer, deformable inclusions in the paste. This reduces the yield stress as shown in Figure 6. The calculation of capillary number as a function of time thus enables an understanding of the rheology of foamed suspensions from those of their skeletal pastes. Even when the yield stress is reduced with increasing surfactant dosage, the printability of the foamed suspensions is not influenced because of their lower density which enables shape retention even at lower yield stresses. The significant drop in the yield stress between a surfactant dosage of 1% and 2% can also be attributed to steric repulsion between the particles in the suspension and the surfactant molecules [55].

⁻

[§] It is assumed for the sake of simplicity that the total pore volume and the pore size in fresh samples are equal to those measured in hardened samples. While mechanisms such as ripening and drainage are likely to influence the pore structure features between fresh and hardened samples, it is ignored in the discussions here.

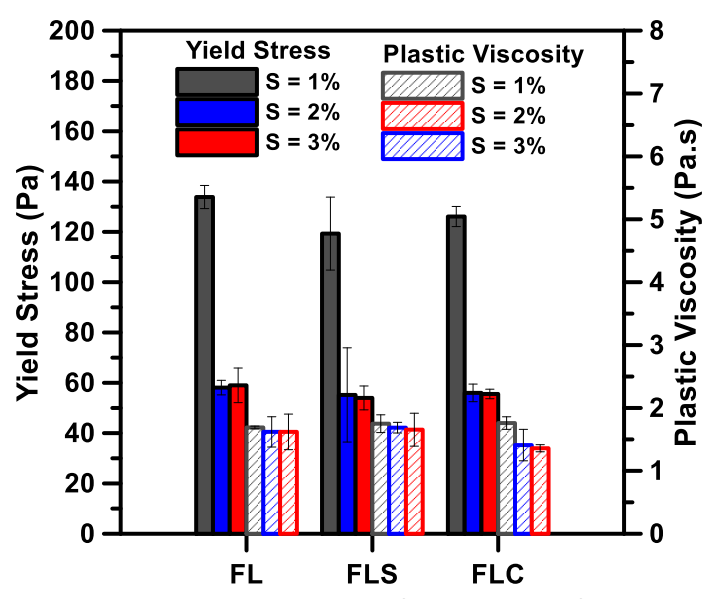


Figure 6: Yield stress and plastic viscosity of the printable foamed suspensions.

3.2 Buildability of Foamed Suspensions

The fresh foamed suspensions must have ability to resist the overburden pressure due to the superimposed printed layers and remain shape stable after printing. This requires the mixtures to be able to recover most of its initial viscosity after the extrusion effect is simulated. Figure 7 depicts the viscosity recovery response of the FL, FLS, and FLC mixtures. These figures indicate three stages of viscosity evolution: the initial viscosity of the suspensions at rest or before extrusion (before printing; from 0 to 60 s), the viscosity of the suspensions during the simulated extrusion process (during printing; 60 s to 90 s), and the viscosity of the simulated extruded suspensions (after printing; 90s to 150 s) as defined in [46,50]. All the foamed suspensions (FL, FLS, and FLC) show a high viscosity at rest and the values dropped significantly when the shear rate was increased to simulate extrusion, as expected. The smooth material flow during extrusion was ensured by the low viscosity. On further lowering of the shear rate, significant recovery of the initial viscosity is noticed, indicating better buildability of the suspensions. Previous work [10,11] have shown that the addition of finer particles like limestone improve the cohesiveness, packing and colloidal interaction thereby providing high initial viscosity and yield stress [59]. For all the three mixtures, the viscosity recovery was in the range of 80% to 95%. The effect of high shear rate that simulates extrusion would have resulted in changes in the fresh state microstructure, that impedes total viscosity recovery. Among the three foamed mixtures, the FLS mixture showed slightly lower retention than the FL mixture. Even at a much lower w/b, the OPC-containing mixture showed similar viscosity recovery, because of the difference in the activating solution characteristics as explained earlier. However, it can be seen that the viscosity recovery for all the mixtures considered here are similar to or higher than those of conventional and geopolymeric 3D-printed pastes reported in literature [46,50], attesting to the buildability of these foamed suspensions.

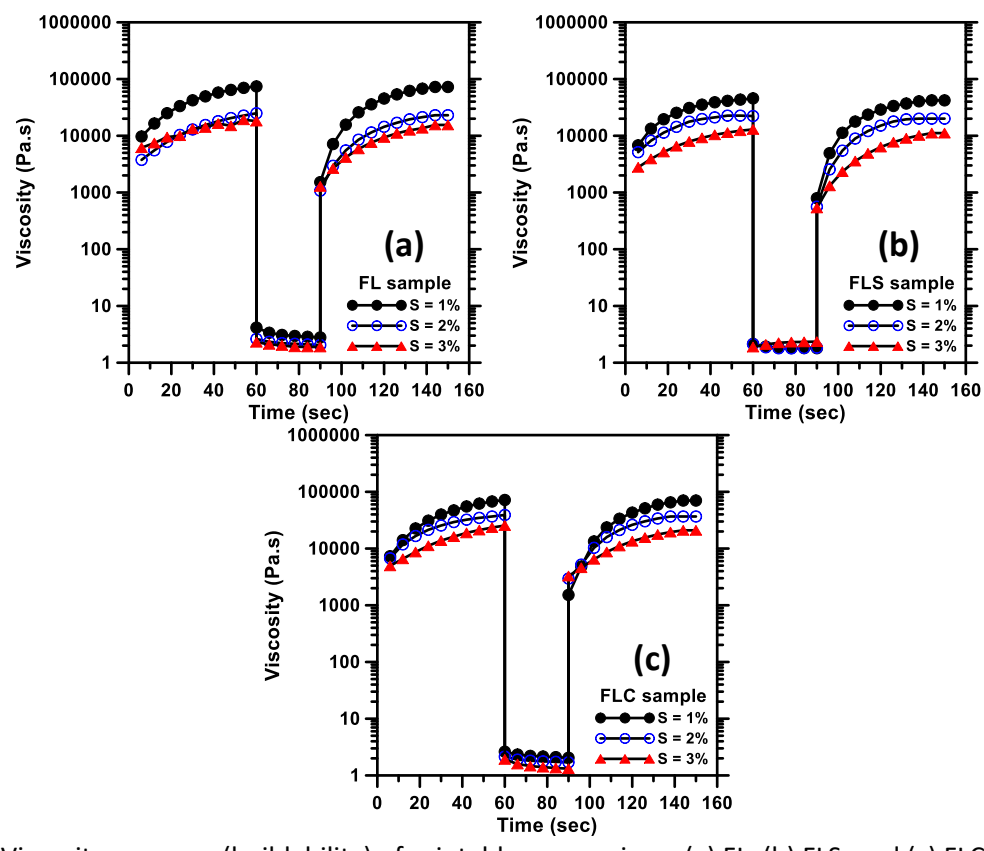


Figure 7: Viscosity recovery (buildability) of printable suspensions: (a) FL, (b) FLS, and (c) FLC mixtures.

A single filament (layer) of each suspension at different surfactant dosages were printed and the shape retention factor of printed filament (SRF) was determined using Equation 2. Figure 8 shows the single printed filaments showing actual layer width after printing (FLS suspension used as an example). The SRF values are reported in Table 3, which roughly scale with the viscosity recovery values described earlier — higher the viscosity retention, higher the SRF. The SRF values are found to decrease with increasing surfactant dosage due to the increased wettability when higher amounts of surfactant are used, which was also evident from the mini-slump values (see Figure 5). Also, the mixtures with 1% surfactant dosage was stiffer than mixtures with 2% and 3% surfactant dosages which explains its better SRF value, as reported in [60].

In addition to a single layer, a single perimeter shape with multiple layers was also printed to represent the buildability of the printable foams as shown in Figure 9. The aspect ratio (overall height to layer width) was found to be 12.5 (25 layers for a total height of ~75 mm) for the mixtures with 1% surfactant dosage, and 8.5 (17 layers for a total height of ~51 mm) for the mixtures with 2%, and 3% surfactant dosages. For

the suspensions with 1% surfactant dosage, particularly with FL and FLC mixtures, the aspect ratio could have been higher but for the printed shape reaching the z-axis limit of the printer used in this study. The layer stability was generally preserved under overburden pressures due to the combined effect of cohesive and uniform suspensions and the fact that the suspensions have very low densities - similar to or lower than that of water (see Table 4), which enabled the layers to withstand the stress from the superimposed layers. The 3% surfactant mixture shown in Figure 9 has the lowest bulk density (Table 4), which has slightly compromised the geometry of the printed shape.

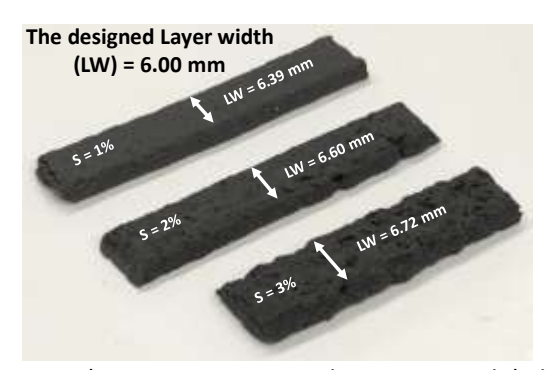


Figure 8: Single printed filaments (FLS suspension used as an example) showing actual layers width after printing.

Table 3: Shape retention factor (SRF) of the foamed suspensions

Mixture ID	Shape retention factor of printed filament (SRF)						
IVIIXTUIE ID	S = 1%	S = 2%	S = 3%				
FL	0.96	0.94	0.92				
FLS	0.94	0.91	0.89				
FLC	0.95	0.92	0.90				

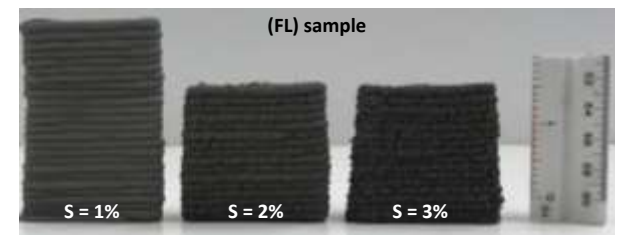


Figure 9: Number of stacked printed layers to evaluate the stability and buildability of foamed suspensions.

3.3 Bulk Densities, Pore Structure, and Microstructure of Foamed Matrices

This section investigates the bulk densities, pore structure, and microstructural features of the 3D-printable foamed matrices developed in this study. Two types of samples were prepared and studied in this section: (i) samples subjected to extrusion during printing, and (ii) samples cast directly in the molds. The influence of the processing method on the physical properties and microstructural features of the foamed matrices are evaluated.

Table 4 shows the specific gravity and bulk densities of extruded and normally cast foamed matrices, measured based on three replicate samples. It can be noticed from the table that the specific gravity of the FLC mixture is the highest while that of FLS, the lowest. The higher specific gravity of the FLC mixture can be attributed to the presence of OPC in this mixture that has the highest specific gravity among the constituents used. The foamed samples showed bulk densities ranging from 0.63 to 1.15 g/cm³ based on the surfactant dosage. The bulk densities are observed to reduce with increasing surfactant dosage, as expected. Here also, the FLC samples show the highest bulk densities. There is virtually no difference in the bulk densities between the extruded and cast samples, implying that the applied extrusion pressure, rate and extruder geometry does not significantly influence the pore structure.

Table 4: Specific gravity and bulk densities of foamed matrices (standard deviation in parentheses based on three replicates)

Samples ID	Specific	Bulk density (g/cm³)							
	gravity	Extr	uded and prin	nted*	Cast in molds**				
	(g/cm^3)	S =1%	S =2%	S =3%	S =1%	S =2%	S =3%		
FL	2.43	0.92	0.72	0.63	0.93	0.71	0.64		
	(0.04)	(0.007)	(0.002)	(0.038)	(0.010)	(0.004)	(0.020)		
FLS	2.37	1.03	0.81	0.67	1.04	0.84	0.68		
	(0.074)	(0.099)	(0.035)	(0.082)	(0.100)	(0.050)	(0.094)		
FLC	2.58	1.15	1.08	0.94	1.16	1.10	0.95		
	(0.078)	(0.055)	(0.099)	(0.086)	(0.070)	(0.097)	(0.074)		

^{*}Samples were exposed to extrusion effect during printing.

The pore structure (total pore volume and critical pore size) of the foamed samples are important in ensuring adequate functional performance, including thermal insulation. Figure 10 depicts the cumulative volume of mercury intruded and the differential mercury intrusion curves for all the printed (extruded) and cast foamed samples. It can be noticed that the cumulative volume intruded and the critical pore size (corresponding to the peak in the differential volume curve, which is indicative of the percolating pore size in the material [61]) increases when the surfactant dosage is increased. It is also observed that the cumulative volume intruded shows only minor differences between the printed (extruded) and cast

^{**}Samples normally poured and cast into molds (not exposed to extrusion effect).

samples, but the critical pore sizes showed an increase (shifted to right) in printed samples as compared to the cast samples. It is important to note that mercury intrusion does not accurately capture pores that are generally greater than ~100 μ m in size, and thus even if such pores collapse under extrusion pressure, it would not be captured using MIP. However, in the range of pore sizes measured by MIP, it is possible that smaller pores coalesce under extrusion pressure, and form larger pores, which is captured through the rightward shift of the differential volume curves corresponding to the extruded samples as shown in Figures 10(d-f). In general, a bimodal pore size distribution with smaller pores in the 0.08-to-0.5 μ m range and larger pores in the 12-to-80 μ m range is observed for the cast samples, while this changes to 0.3-to-0.8 μ m range and 20-to-100 μ m range for the extruded samples. The pore size distribution and the similarity in the cumulative intrusion curves show that the extrusion process does not significantly influence the stability of the pore network.

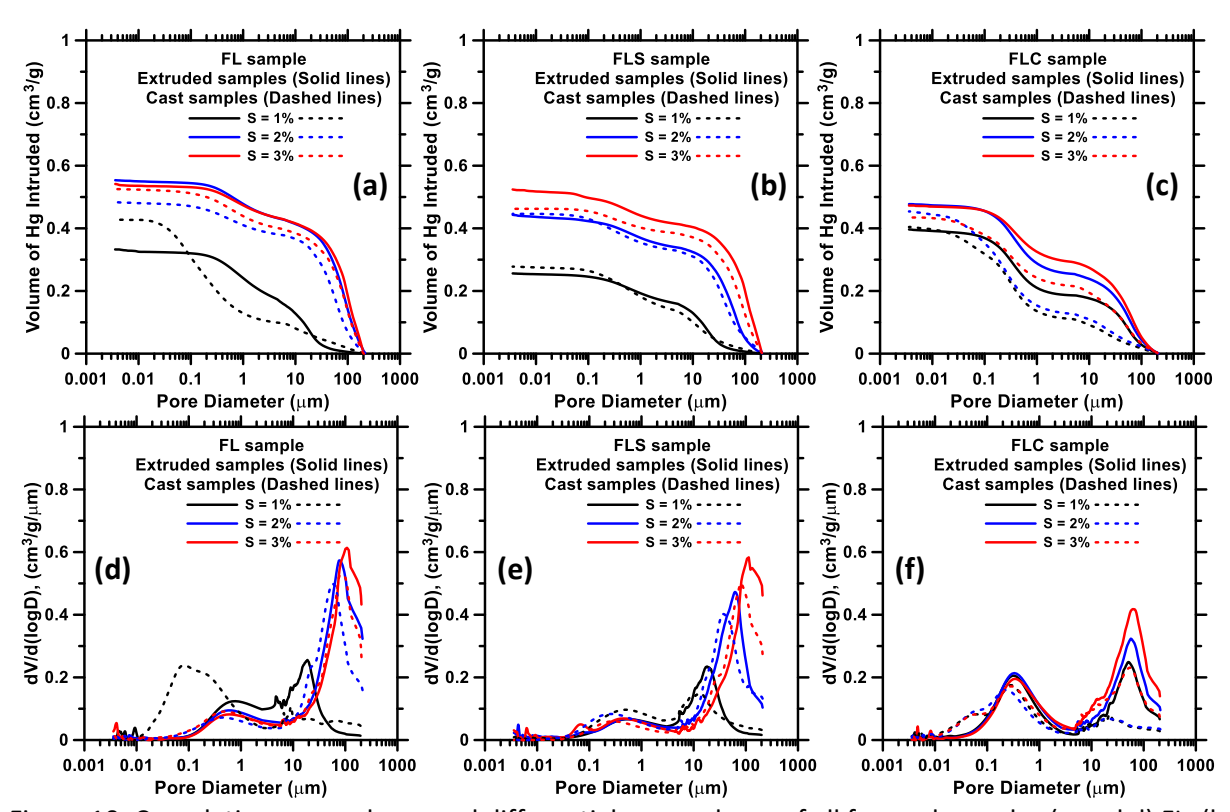


Figure 10: Cumulative pore volume and differential pore volume of all foamed samples (a and d) FL, (b and e) FLS, and (c and f) FLC samples. (Extruded samples represented by solid lines and cast samples represented by dashed lines).

Scanning electron micrographs of the extruded FL mixture is shown in Figure 11, for all the three surfactant dosages. The micrographs clearly show the distribution of macropores. The increase in pore volumes and the pore morphology as a function of surfactant dosage are clearly depicted in this figure. The jamming transition (~0.64) in 3D foams corresponds to random close packed density for hard spheres

[62,63]. However, for the soft spheres, foam volume fraction above the jamming transition indicates that the voids have to deform or interpenetrate (see the associated rheological discussion earlier). Careful observation of Figure 11 for mixtures with higher surfactant content reveals this aspect. Since larger pores that cannot be detected using MIP will be present in these mixtures, the total porosities of the samples were determined using Equation 6, while the MIP porosities were determined using the cumulative volume intruded and the bulk densities of the samples. Figure 12(a) depicts the total porosity and the porosity extracted from MIP for the extruded samples, showing that MIP accounts for only about 50-60% of the total pore volume in the FL and FLS mixtures. For the FLC mixtures, the presence of OPC and the much lower w/b results in generally lower pore sizes, and thus the MIP porosity is similar to that determined using Equation 6. Figure 12(b) shows the relationship between the bulk densities and porosities. The FL and FLS mixtures show similar trends while the FLC mixture shows a slightly different trend, because of reasons described above.

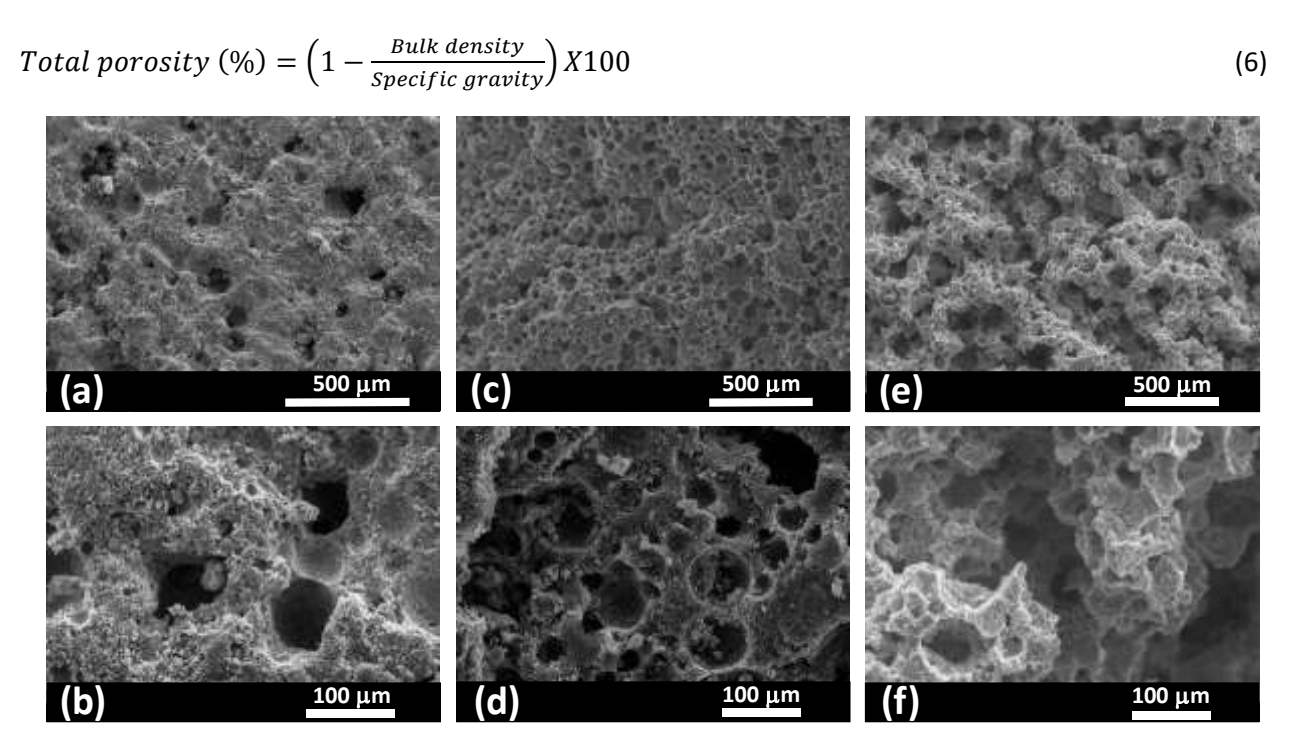


Figure 11: SEM micrographs at two different magnifications of microstructure of the extruded FL sample at different surfactant dosages (a and b) S = 1%, (c and d) S = 2%, and (e and f) S = 3%.

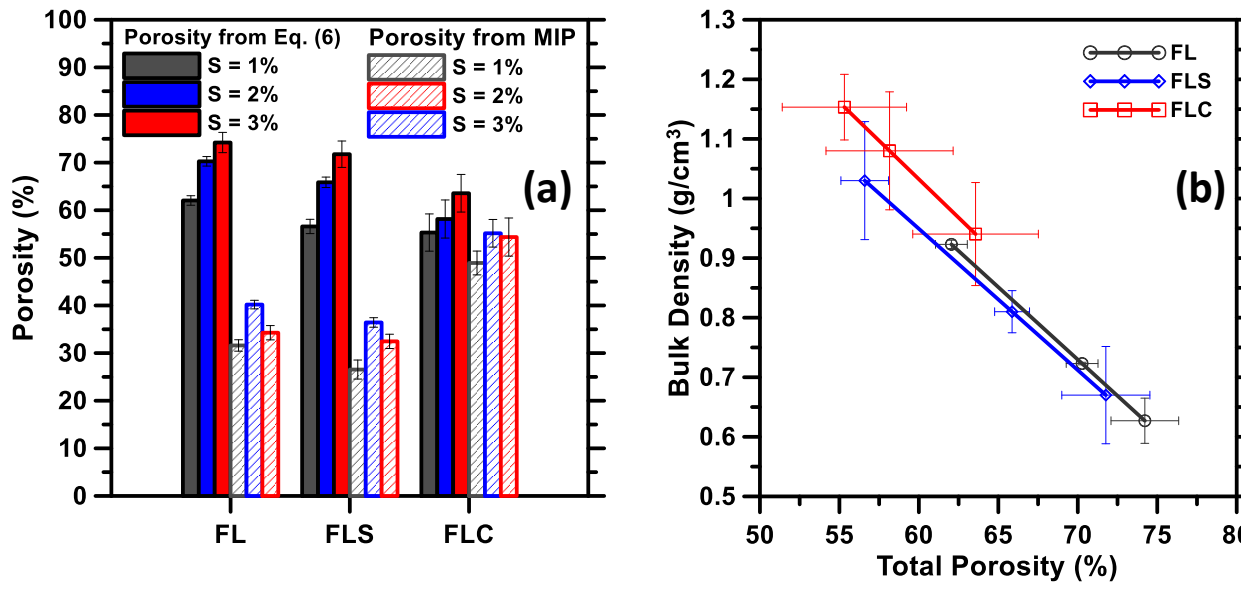


Figure 12: (a) Total theoretical porosity calculated from Equation 6 and the porosity obtained from MIP, and (b) relationship between the total porosity and bulk densities of printed foamed samples.

3.4 Thermal Properties of Foamed Matrices and Design of Energy-Efficient Envelope Materials

The thermal conductivities of the printed foamed matrices were determined from the OPC plate-foam composite specimens using a series rule of mixtures approach. Figure 13(a) depicts the thermal conductivity of the printed foamed samples along with the thermal conductivity of an OPC paste (w/c of 0.40) while Figure 13(b) shows the relationship between the thermal conductivities and bulk densities of the printed foamed matrices. Samples with higher content of surfactant yielded lower thermal conductivities because of their higher porosities. The relationship between porosity and thermal conductivity is shown in Figure 13(b). The thermal conductivity of the printed foamed matrices are similar to other insulating materials including aerated/foamed concrete, expanded clay, cork boards etc. as well as porous fly ash based geopolymers reported in [33,64,65].

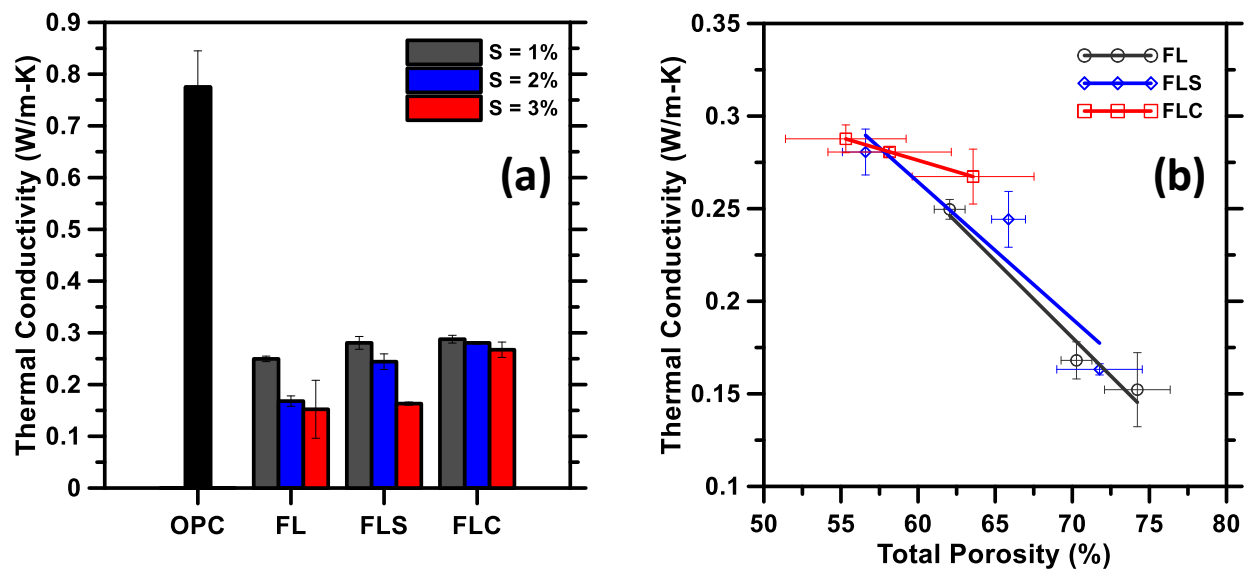


Figure 13: (a) Thermal conductivity of all printed foamed matrices and the OPC plain paste, and (b) relationship between porosity and thermal conductivity of all printed foamed samples.

As noticed from Figure 13, the printed geopolymer foams exhibit low thermal conductivities, but these values are higher than those of commonly used building insulation materials such as mineral wool, expanded or extruded polystyrene (EPS/XPS), or polyisocyanurate which are generally lower than 0.05 W/m-K. However, it is possible to reduce the thermal conductivity of the entire insulation layer in insulated sandwich concrete wall panels by careful architecture of the geopolymeric foam, which is enabled by 3D printing (see Figure 1). 3D-printed precast concrete insulated wall panels can thus be produced with two layers of concrete separated by printed geopolymeric foam of suitable architecture, examples of which were shown in Figure 1. The properties and geometry of the concrete wythes (external layers of concrete that provides structural resistance) and the foam layer can be designed based on the structural and functional requirements of the building.

To demonstrate the effectiveness of 3D-printed geopolymer foam layers for insulated wall panels, the FL mixture with 3% surfactant dosage is considered, which has a thermal conductivity of 0.15 W/m-K. As shown in Figure 1, this mixture can be printed on a concrete backing as a prototype for an insulated sandwich wall panel. The printed material in Figure 1 occupies only 50% of the volume with the remaining being air of low thermal conductivity (0.0257 W/m-K). Using several analytical models for effective thermal conductivity including the simple series and parallel models, Maxwell model, and effective media theory (EMT) [54,66,67], the effective thermal conductivities determined as a function of volume fraction of air (this does not include the voids in the foams themselves since they are accounted for in the measured thermal conductivity of the foam) are shown in Figure 14. The horizontal line corresponds to

the desired thermal conductivity of the foam layer, to match that of commercially available insulation materials. It can be seen that, with an air volume fraction of ~60-70% (i.e., printed solid volume fraction of 30-40%), EMT predicts that the geopolymeric foam layer will have a thermal conductivity similar to that of commercial insulation materials. This analysis does not consider the system to be a dual-porosity media composed of smaller pores within the foam and larger spaces between the foam layers. The interface effects that hinder heat conduction are not considered, rendering the determined values to be more conservative. Moreover, the printing architecture can also be tailored to change the interface areas or lengths of heat transport path to induce more losses, and thus enhance insulation.

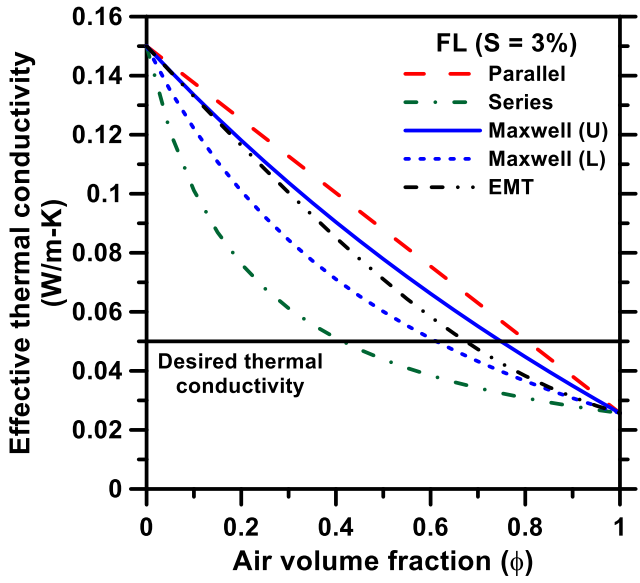


Figure 14: Model-based determinations of effective thermal conductivity of geopolymeric foam layers printed with air gaps.

4. Summary and Conclusions

This paper has presented an extrusion-based 3D-printing technique to create geopolymeric foams for thermal insulation applications. A novel synthesis method using different surfactant contents where foam jamming transition is achieved through multiple mixing steps has been detailed. Improvements in microstructural packing that reinforces the solid skeleton also contributed to ensuring the stability of the foamed matrices when subjected to extrusion. The final ingredients of the foamed suspensions included fly ash, limestone and silica fume or OPC. The activators used were sodium silicate and NaOH or sodium sulfate. All the foamed matrices were designed to have bulk densities lower than that of water, and unsurprisingly, increase in surfactant dosage resulted in significantly reduced bulk densities of the printed foams.

Mini-slump test was used to obtain preliminary indications of shape stability, and single printed filaments were used to determine the shape retention factor. The shear yield stress of the chosen suspensions ranged from 60 to 130 Pa; the higher the surfactant dosage, the lower the yield stress. Below the foam jamming transition, the bubbles acted as hard spheres that enhance the yield stress while below the jamming transition, they were able to deform, which was shown through the capillary number. The lower yield stress of the foamed suspensions did not influence their buildability because of their lower density. The buildability was explicitly determined using viscosity response of the suspensions after subjecting them to simulated extrusion through changes in the shear rate. The low viscosity under extrusion (high shear rates) enabled smooth and continuous printing without any defects. The viscosity recovery of the chosen foamed matrices were high, demonstrating excellent buildability, which was verified through printing multiple layers and determining the aspect ratio (ratio of overall height to later width) of the printed structure. It was noted that the layer stability was preserved under the weight of the superimposed layers due to the combined effect of cohesive mixtures with high skeletal densities due to microstructural packing and low overall densities due to the stable bubbles. The differences in bulk densities between the extruded samples and normally cast samples were minimal, alluding to the fact that the extrusion process did not significantly change the overall pore volume in the foamed mixtures. However, mercury intrusion porosimetry identified slight increase in the critical pore sizes of extruded samples as compared to normally cast samples, indicating some coalescence of smaller pores under extrusion.

The thermal conductivities of the foamed matrices ranged between 0.15 and 0.25 W/m-K, for porosities ranging from 55-75%. These values are significantly lower than those of conventional cement pastes (~0.8-to-1.0 W/m-K), but higher than those of commonly used insulation materials including polystyrene and mineral wool (~0.05 W/m-K). To enable substitution of conventional insulation materials with 3D-printed geopolymeric foam in sandwich wall panels, this study has proposed the use of 3D-printed foam layer architecture in such a way that dual-porosity systems - with smaller pores in the foam and larger pores in between the printed paths - can be achieved. Using effective medium theory, it has been shown that if the printed structure has an overall volume fraction of 60-70% (excluding the voids in the foam matrix itself), the effective thermal conductivity of the system approaches that of a commercial insulation material. Thus, 3D-printing of geopolymeric foams can be used in conjunction with precast wall manufacturing (which could also be 3D printed) to develop economical and sustainable structural systems that compare with existing systems with respect to thermal insulation capacity.

5. Acknowledgments

The authors sincerely acknowledge support from National Science Foundation (CMMI: 1727445) towards the conduct of this study. The contents of this paper reflect the views of the authors who are responsible for the facts and accuracy of the data presented herein, and do not necessarily reflect the views and policies of NSF, nor do the contents constitute a standard, specification or a regulation. We gratefully acknowledge the use of facilities within Laboratory for the Science of Sustainable Infrastructural Materials (LS-SIM) at Arizona State University.

6. References

- [1] G. De Schutter, K. Lesage, V. Mechtcherine, V.N. Nerella, G. Habert, I. Agusti-Juan, Vision of 3D printing with concrete Technical, economic and environmental potentials, Cement and Concrete Research. 112 (2018) 25–36. doi:10.1016/j.cemconres.2018.06.001.
- [2] D. Asprone, F. Auricchio, C. Menna, V. Mercuri, 3D printing of reinforced concrete elements: Technology and design approach, Construction and Building Materials. 165 (2018) 218–231. doi:10.1016/j.conbuildmat.2018.01.018.
- [3] I. Hager, A. Golonka, R. Putanowicz, 3D Printing of Buildings and Building Components as the Future of Sustainable Construction?, Procedia Engineering. 151 (2016) 292–299. doi:10.1016/j.proeng.2016.07.357.
- [4] R.A. Buswell, W.R. Leal de Silva, S.Z. Jones, J. Dirrenberger, 3D printing using concrete extrusion: A roadmap for research, Cement and Concrete Research. 112 (2018) 37–49. doi:10.1016/j.cemconres.2018.05.006.
- [5] P. Marks, The many flavours of printing in 3D, New Scientist. 211 (2011) 18. doi:10.1016/S0262-4079(11)61818-6.
- [6] P. Wu, J. Wang, X. Wang, A critical review of the use of 3-D printing in the construction industry, Automation in Construction. 68 (2016) 21–31. doi:10.1016/j.autcon.2016.04.005.
- [7] C. Gosselin, R. Duballet, Ph. Roux, N. Gaudillière, J. Dirrenberger, Ph. Morel, Large-scale 3D printing of ultra-high performance concrete a new processing route for architects and builders, Materials & Design. 100 (2016) 102–109. doi:10.1016/j.matdes.2016.03.097.
- [8] M. Hambach, D. Volkmer, Properties of 3D-printed fiber-reinforced Portland cement paste, Cement and Concrete Composites. 79 (2017) 62–70. doi:10.1016/j.cemconcomp.2017.02.001.
- [9] A. Kazemian, X. Yuan, E. Cochran, B. Khoshnevis, Cementitious materials for construction-scale 3D printing: Laboratory testing of fresh printing mixture, Construction and Building Materials. 145 (2017) 639–647. doi:10.1016/j.conbuildmat.2017.04.015.
- [10] H. Alghamdi, S.A.O. Nair, N. Neithalath, Insights into material design, extrusion rheology, and properties of 3D-printable alkali-activated fly ash-based binders, Materials & Design. 167 (2019) 107634. doi:10.1016/j.matdes.2019.107634.
- [11] S.A.O. Nair, H. Alghamdi, A. Arora, I. Mehdipour, G. Sant, N. Neithalath, Linking fresh paste microstructure, rheology and extrusion characteristics of cementitious binders for 3D printing, Journal of the American Ceramic Society. 0 (2018). doi:10.1111/jace.16305.
- [12] B. Panda, G.B. Singh, C. Unluer, M.J. Tan, Synthesis and characterization of one-part geopolymers for extrusion based 3D concrete printing, Journal of Cleaner Production. 220 (2019) 610–619. doi:10.1016/j.jclepro.2019.02.185.

- [13] N. Roussel, Rheological requirements for printable concretes, Cement and Concrete Research. 112 (2018) 76–85. doi:10.1016/j.cemconres.2018.04.005.
- [14] D. Marchon, S. Kawashima, H. Bessaies-Bey, S. Mantellato, S. Ng, Hydration and rheology control of concrete for digital fabrication: Potential admixtures and cement chemistry, Cement and Concrete Research. 112 (2018) 96–110. doi:10.1016/j.cemconres.2018.05.014.
- [15] L. Reiter, T. Wangler, N. Roussel, R.J. Flatt, The role of early age structural build-up in digital fabrication with concrete, Cement and Concrete Research. 112 (2018) 86–95. doi:10.1016/j.cemconres.2018.05.011.
- [16] S.C. Paul, G.P.A.G. van Zijl, M.J. Tan, I. Gibson, A review of 3D concrete printing systems and materials properties: current status and future research prospects, Rapid Prototyping Journal. 24 (2018) 784–798. doi:10.1108/RPJ-09-2016-0154.
- [17] M. Ashraf, I. Gibson, M.G. Rashed, CHALLENGES AND PROSPECTS OF 3D PRINTING IN STRUCTURAL ENGINEERING, 13th International Conference on Steel, Space and Composite Structures (Perth, WA). (2018) 11.
- [18] Y.W.D. Tay, M.Y. Li, M.J. Tan, Effect of printing parameters in 3D concrete printing: Printing region and support structures, Journal of Materials Processing Technology. 271 (2019) 261–270. doi:10.1016/j.jmatprotec.2019.04.007.
- [19] B. Panda, S.C. Paul, L.J. Hui, Y.W.D. Tay, M.J. Tan, Additive manufacturing of geopolymer for sustainable built environment, Journal of Cleaner Production. 167 (2017) 281–288. doi:10.1016/j.jclepro.2017.08.165.
- [20] B. Panda, S. Chandra Paul, M. Jen Tan, Anisotropic mechanical performance of 3D printed fiber reinforced sustainable construction material, Materials Letters. 209 (2017) 146–149. doi:10.1016/j.matlet.2017.07.123.
- [21] L. Jiang, H. Xiao, W. An, Y. Zhou, J. Sun, Correlation study between flammability and the width of organic thermal insulation materials for building exterior walls, Energy and Buildings. 82 (2014) 243–249. doi:10.1016/j.enbuild.2014.06.013.
- [22] A.A. Stec, T.R. Hull, Assessment of the fire toxicity of building insulation materials, Energy and Buildings. 43 (2011) 498–506. doi:10.1016/j.enbuild.2010.10.015.
- [23] Y. Ai-hua, L. Jian-yong, Z. Xia, Y. Zhan, Study of the Combustion Performance of Three Kinds of Organic Heat Insulation Materials, Procedia Engineering. 11 (2011) 614–619. doi:10.1016/j.proeng.2011.04.704.
- [24] A. Vyatskikh, A. Kudo, S. Delalande, J.R. Greer, Additive Manufacturing of Polymer-Derived Titania for One-Step Solar Water Purification, Materials Today Communications. (2018). doi:10.1016/j.mtcomm.2018.02.010.
- [25] Y. Chen, H. Yao, L. Wang, Acoustic band gaps of three-dimensional periodic polymer cellular solids with cubic symmetry, Journal of Applied Physics. 114 (2013) 043521. doi:10.1063/1.4817168.
- [26] Y. Chen, F. Qian, L. Zuo, F. Scarpa, L. Wang, Broadband and multiband vibration mitigation in lattice metamaterials with sinusoidally-shaped ligaments, Extreme Mechanics Letters. 17 (2017) 24–32. doi:10.1016/j.eml.2017.09.012.
- [27] M.L. Lifson, M.-W. Kim, J.R. Greer, B.-J. Kim, Enabling Simultaneous Extreme Ultra Low-k in Stiff, Resilient, and Thermally Stable Nano-Architected Materials, Nano Lett. 17 (2017) 7737–7743. doi:10.1021/acs.nanolett.7b03941.
- [28] C. Minas, D. Carnelli, E. Tervoort, A.R. Studart, 3D Printing of Emulsions and Foams into Hierarchical Porous Ceramics, Advanced Materials. 28 (2016) 9993–9999. doi:10.1002/adma.201603390.
- [29] B.G. Compton, J.A. Lewis, 3D-Printing of Lightweight Cellular Composites, Advanced Materials. 26 (2014) 5930–5935. doi:10.1002/adma.201401804.

- [30] A.K. Singh, B. Patil, N. Hoffmann, B. Saltonstall, M. Doddamani, N. Gupta, Additive Manufacturing of Syntactic Foams: Part 1: Development, Properties, and Recycling Potential of Filaments, JOM. 70 (2018) 303–309. doi:10.1007/s11837-017-2734-7.
- [31] A.K. Singh, B. Saltonstall, B. Patil, N. Hoffmann, M. Doddamani, N. Gupta, Additive Manufacturing of Syntactic Foams: Part 2: Specimen Printing and Mechanical Property Characterization, JOM. 70 (2018) 310–314. doi:10.1007/s11837-017-2731-x.
- [32] G. Masi, W.D.A. Rickard, L. Vickers, M.C. Bignozzi, A. van Riessen, A comparison between different foaming methods for the synthesis of light weight geopolymers, Ceramics International. 40 (2014) 13891–13902. doi:10.1016/j.ceramint.2014.05.108.
- [33] H. Alghamdi, N. Neithalath, Novel synthesis of lightweight geopolymer matrices from fly ash through carbonate-based activation, Materials Today Communications. 17 (2018) 266–277. doi:10.1016/j.mtcomm.2018.09.014.
- [34] H. Alghamdi, A. Dakhane, A. Alum, M. Abbaszadegan, B. Mobasher, N. Neithalath, Synthesis and characterization of economical, multi-functional porous ceramics based on abundant aluminosilicates, Materials & Design. 152 (2018) 10–21. doi:10.1016/j.matdes.2018.04.060.
- [35] C. Bai, P. Colombo, High-porosity geopolymer membrane supports by peroxide route with the addition of egg white as surfactant, Ceramics International. 43 (2017) 2267–2273. doi:10.1016/j.ceramint.2016.10.205.
- [36] C. Bai, G. Franchin, H. Elsayed, A. Zaggia, L. Conte, H. Li, P. Colombo, High-porosity geopolymer foams with tailored porosity for thermal insulation and wastewater treatment, Journal of Materials Research. 32 (2017) 3251–3259. doi:10.1557/jmr.2017.127.
- [37] S. Swarup, C.K. Schoff, A survey of surfactants in coatings technology, Progress in Organic Coatings. 23 (1993) 1–22. doi:10.1016/0033-0655(93)80002-R.
- [38] M. Strozi Cilla, P. Colombo, M. Raymundo Morelli, Geopolymer foams by gelcasting, Ceramics International. 40 (2014) 5723–5730. doi:10.1016/j.ceramint.2013.11.011.
- [39] S. Guignot, S. Faure, M. Vignes-Adler, O. Pitois, Liquid and particles retention in foamed suspensions, Chemical Engineering Science. 65 (2010) 2579–2585. doi:10.1016/j.ces.2009.12.039.
- [40] I. Lesov, S. Tcholakova, N. Denkov, Drying of particle-loaded foams for production of porous materials: mechanism and theoretical modeling, RSC Advances. 4 (2014) 811–823. doi:10.1039/C3RA44500C.
- [41] L. Du, K.J. Folliard, Mechanisms of air entrainment in concrete, Cement and Concrete Research. 35 (2005) 1463–1471. doi:10.1016/j.cemconres.2004.07.026.
- [42] D. Weaire, S. Hutzler, The physics of foams, Clarendon, 1999.
- [43] D. Langevin, Aqueous foams and foam films stabilised by surfactants. Gravity-free studies, Comptes Rendus Mécanique. 345 (2017) 47–55. doi:10.1016/j.crme.2016.10.009.
- [44] A. Dakhane, S. Tweedley, S. Kailas, R. Marzke, N. Neithalath, Mechanical and microstructural characterization of alkali sulfate activated high volume fly ash binders, Materials & Design. 122 (2017) 236–246. doi:10.1016/j.matdes.2017.03.021.
- [45] Slic3r, (2017). http://slic3r.org/.
- [46] B. Panda, M.J. Tan, Experimental study on mix proportion and fresh properties of fly ash based geopolymer for 3D concrete printing, Ceramics International. 44 (2018) 10258–10265. doi:10.1016/j.ceramint.2018.03.031.
- [47] K. Vance, G. Sant, N. Neithalath, The rheology of cementitious suspensions: A closer look at experimental parameters and property determination using common rheological models, Cement and Concrete Composites. 59 (2015) 38–48. doi:10.1016/j.cemconcomp.2015.03.001.
- [48] K. Vance, A. Arora, G. Sant, N. Neithalath, Rheological evaluations of interground and blended cement–limestone suspensions, Construction and Building Materials. 79 (2015) 65–72. doi:10.1016/j.conbuildmat.2014.12.054.

- [49] I. Lesov, S. Tcholakova, N. Denkov, Factors controlling the formation and stability of foams used as precursors of porous materials, Journal of Colloid and Interface Science. 426 (2014) 9–21. doi:10.1016/j.jcis.2014.03.067.
- [50] B. Panda, C. Unluer, M.J. Tan, Investigation of the rheology and strength of geopolymer mixtures for extrusion-based 3D printing, Cement and Concrete Composites. 94 (2018) 307–314. doi:10.1016/j.cemconcomp.2018.10.002.
- [51] T. Bakharev, Thermal behaviour of geopolymers prepared using class F fly ash and elevated temperature curing, Cement and Concrete Research. 36 (2006) 1134–1147. doi:10.1016/j.cemconres.2006.03.022.
- [52] K. Okada, A. Ooyama, T. Isobe, Y. Kameshima, A. Nakajima, K.J.D. MacKenzie, Water retention properties of porous geopolymers for use in cooling applications, Journal of the European Ceramic Society. 29 (2009) 1917–1923. doi:10.1016/j.jeurceramsoc.2008.11.006.
- [53] P. Rovnaník, Effect of curing temperature on the development of hard structure of metakaolin-based geopolymer, Construction and Building Materials. 24 (2010) 1176–1183. doi:10.1016/j.conbuildmat.2009.12.023.
- [54] M. Aguayo, S. Das, C. Castro, N. Kabay, G. Sant, N. Neithalath, Porous inclusions as hosts for phase change materials in cementitious composites: Characterization, thermal performance, and analytical models, Construction and Building Materials. 134 (2017) 574–584. doi:10.1016/j.conbuildmat.2016.12.185.
- [55] B. Feneuil, O. Pitois, N. Roussel, Effect of surfactants on the yield stress of cement paste, Cement and Concrete Research. 100 (2017) 32–39. doi:10.1016/j.cemconres.2017.04.015.
- [56] R. Prud'homme, Foams: Theory: Measurements: Applications, Routledge, 2017.
- [57] L. Ducloué, O. Pitois, L. Tocquer, J. Goyon, G. Ovarlez, Yielding and flow of foamed metakaolin pastes, Colloids and Surfaces A: Physicochemical and Engineering Aspects. 513 (2017) 87–94. doi:10.1016/j.colsurfa.2016.11.015.
- [58] L. Ducloué, O. Pitois, J. Goyon, X. Chateau, G. Ovarlez, Rheological behaviour of suspensions of bubbles in yield stress fluids, Journal of Non-Newtonian Fluid Mechanics. 215 (2015) 31–39.
- [59] R.J. Flatt, P. Bowen, Yodel: A Yield Stress Model for Suspensions, Journal of the American Ceramic Society. 89 (2006) 1244–1256. doi:10.1111/j.1551-2916.2005.00888.x.
- [60] B. Panda, J.H. Lim, M.J. Tan, Mechanical properties and deformation behaviour of early age concrete in the context of digital construction, Composites Part B: Engineering. 165 (2019) 563–571. doi:10.1016/j.compositesb.2019.02.040.
- [61] P.A. Webb, An Introduction To The Physical Characterization of Materials by Mercury Intrusion Porosimetry with Emphasis On Reduction And Presentation of Experimental Data, Micromeritics Instrument Corp., Norcross, Georgia. (2001).
- [62] J.D. Bernal, J. Mason, Packing of spheres: co-ordination of randomly packed spheres, Nature. 4754 (1960) 910.
- [63] A. Donev, F.H. Stillinger, S. Torquato, Unexpected density fluctuations in jammed disordered sphere packings, Physical Review Letters. 95 (2005).
- [64] Z. Zhang, J.L. Provis, A. Reid, H. Wang, Mechanical, thermal insulation, thermal resistance and acoustic absorption properties of geopolymer foam concrete, Cement and Concrete Composites. 62 (2015) 97–105. doi:10.1016/j.cemconcomp.2015.03.013.
- [65] R.M. Novais, L.H. Buruberri, G. Ascensão, M.P. Seabra, J.A. Labrincha, Porous biomass fly ash-based geopolymers with tailored thermal conductivity, Journal of Cleaner Production. 119 (2016) 99–107. doi:10.1016/j.jclepro.2016.01.083.
- [66] B. Troschke, H. Burkhardt, Thermal conductivity models fro two-phase systems, Physics and Chemistry of the Earth. 23 (1998) 351–355. doi:10.1016/S0079-1946(98)00036-6.

[67] M.M. Awad, Y.S. Muzychka, Effective property models for homogeneous two-phase flows, Experimental Thermal and Fluid Science. 33 (2008) 106–113. doi:10.1016/j.expthermflusci.2008.07.006.